

# Measuring vacancy-type defect density in monolayer MoS<sub>2</sub>

Aleksandar Radić<sup>†,\*</sup>, Nick von Jeinsen<sup>†</sup>, Vivian Perez<sup>†</sup>, Ke Wang<sup>†</sup>, Min Lin<sup>†</sup>, Boyao Liu<sup>†</sup>, Yiru Zhu<sup>‡</sup>, Ismail Sami<sup>‡</sup>, Kenji Watanabe<sup>§</sup>, Takashi Taniguchi<sup>^</sup>, David Ward<sup>†</sup>, Andrew Jardine<sup>†</sup>, Akshay Rao<sup>†</sup>, Manish Chhowalla<sup>‡,\*</sup>, Sam Lambrick<sup>†,\*</sup>

Author affiliations:

<sup>†</sup>Cavendish Laboratory, Department of Physics, University of Cambridge, JJ Thomson Ave, Cambridge, United Kingdom

<sup>‡</sup>Department of Materials Science and Metallurgy, University of Cambridge, 27 Charles Babbage Road, Cambridge, United Kingdom

<sup>§</sup>Research Center for Electronic and Optical Materials, National Institute for Materials Science, 1-1 Namiki, Tsukuba 305-0044, Japan

<sup>^</sup>Research Center for Materials Nanoarchitectonics, National Institute for Materials Science, 1-1 Namiki, Tsukuba 305-0044, Japan

<sup>\*</sup>Author emails: [ar2071@cam.ac.uk](mailto:ar2071@cam.ac.uk), [mc209@cam.ac.uk](mailto:mc209@cam.ac.uk), [sml59@cantab.ac.uk](mailto:sml59@cantab.ac.uk)

## Abstract

Two-dimensional (2D) materials are being widely researched for their interesting electronic properties. Their optoelectronic, mechanical and thermal properties can be finely modulated using a variety of methods, including strain, passivation, doping, and tuning of defect density. However, measuring defect densities, such as those associated with vacancy-type point defects, is inherently very difficult in atomically thin materials. Here we show that helium atom micro-diffraction can be used to measure defect density in  $\sim 15 \times 20 \mu\text{m}$  monolayer MoS<sub>2</sub>, a prototypical 2D semiconductor, quickly and easily compared to standard methods. We present a simple analytic model, the lattice gas equation, that fully captures the relationship between atomic Bragg diffraction intensity and defect density. The model, combined with ab initio scattering calculations, shows that our technique can immediately be applied to a wide range of 2D materials, independent of sample chemistry or structure. Additionally, favourable signal scaling with lateral resolution makes wafer-scale characterisation immediately possible.

## Introduction

Control of defect density in semiconductors is essential for both current and future optoelectronic devices. In particular, the properties of two-dimensional semiconductors, such as the prototypical MoS<sub>2</sub>, can be tuned using single-atom defects[1] for catalysis[2] and optoelectronic applications[3], [4], [5]. The density of defects is often critical in device design, where precise control of the defect density is necessary to produce the desired device properties reproducibly[6]. However, quantification of defect densities in 2D materials remains a significant experimental challenge, with typically used methods (see Table S1) being low temperature photoluminescence (PL), beamline XPS [6] and STEM[2], with conductive AFM (cAFM)[7] being explored recently. However, all these methods commonly require complicated sample preparation processes, long measurement or beam line access times and can be prohibitively expensive. As such, there is a characterisation shortcoming that will only grow as devices using defect-tuned 2D materials[8] gain further traction in both academic research and industry.

Defect characterisation over wafer-scale monolayers, that are crucial for commercial and industrial uptake of 2D materials, is particularly difficult with existing techniques. We demonstrate helium atom micro-diffraction (HAMD) on device-scale (few micron) monolayer MoS<sub>2</sub> that represents the most challenging implementation of the method due to unfavourable scaling between signal ( $I$ ) and beam spot-size ( $r$ ),  $I \propto 1/r^4$  in a pinhole microscope[9]. Due to this scaling relationship, large area characterisations are not only possible, but favourable using our method. Furthermore, we show that our method can immediately be applied to all 2D materials, independent of sample chemistry or optoelectronic properties.

## Helium atom micro-diffraction

Thermal energy, neutral helium atoms provide a uniquely surface sensitive probe that has an interaction cross-section that is fundamentally independent from a sample's bulk. The helium scatters from the valence electron density of the surface with a classical turning point  $\sim 2\text{-}3 \text{ \AA}$  above the ionic cores[10]. This means that the scattered helium signal is independent of sample thickness, unlike alternative techniques that use photon or electron probes. Thus, the helium signal is solely a function of the electronic order at the surface with no beam penetration to sub-surface layers, making it ideal for the characterization of 2D, soft and electrically sensitive materials, regardless of their bandgap, without sample damage or need for specific sample preparation[11], [12], [13], [14], [15], [16], [17]. Additionally, thermal energy helium beams are

highly sensitive to atomic-scale features due to their commensurate de Broglie wavelength ( $\sim 0.06\text{nm}$  at  $64\text{meV}$ ) and the strong attractive component of the helium-surface interaction potential[18]. The cross sections to monatomic/diatomic adsorbates are therefore many times larger than a typical unit cell, ranging from  $30 - 200\text{\AA}^2$ [19]. One can expect, therefore, that the scattering cross-section between helium and an atomic vacancy would be similarly enhanced.

Recent work has shown that existing scanning helium microscopes (SHeM)[11], [12], [15], [20] can perform Bragg diffraction to determine the crystallographic structure of a surface with few-micron spatial resolution[21], [22]. This technique is termed helium atom micro-diffraction (HAMD).

In this work, we employ HAMD to measure the vacancy-type defect density in monolayer  $\text{MoS}_2$  with zero damage or specific sample preparation. We also present a simple analytic model that decoded defect density from atomic Bragg diffraction, along with computations that, together, validate that our method can immediately be applied to a wide range of materials, independent of sample chemistry or structure.

## Decoding defect density from atomic Bragg diffraction

A helium matter wave can diffract from the surface corrugation created by the valence electron density of the solid, as shown in figure 1 (a), resulting in Bragg diffraction that encodes atomic scale information on the surface structure[19]. Crucially, helium scatters from the valence electron density so that it measures long-range electronic order directly. Measurement of long-range electronic order is the ultimate determining factor in a material's optical and electronic properties, allowing helium scattering to directly probe that which determines final device properties. Historically such measurements were limited to millimetre-scale, carefully prepared, single crystal samples, however, recent advances in instrumentation[21] have allowed atom diffraction to be applied to microscopic, micron-scale samples for the first time, with a  $5\mu\text{m}$  beam used in this study. A helium diffraction pattern is measured by scanning the scattered helium flux (with a high-sensitivity custom atom detector[23]) as a function of the in-plane momentum transfer,  $\Delta K(\theta)$ , as well as the various azimuths on a crystal surface. In our instrument (schematic shown in figure 1 (a)) we use manipulations of the sample position and orientation to allow scanning through the outgoing beam angle,  $\theta$ , and hence  $\Delta K$ . By using a SHeM to perform HAMD we can also switch to imaging mode, allowing us to acquire diffraction contrast[21], [24] optimized helium micrographs. A micrograph of a sample used in the current work is shown in figure 2 (c) alongside an optical image in figure 2 (b) for comparison. Strong contrast is seen between the  $\text{MoS}_2$  and hBN, which both exhibit ordered scattering, while the silicon oxide substrate, which scatters diffusely[25], appears dark. Full details on the sample materials, geometry and effect of substrate are contained in the Materials and Methods supplementary materials.

Defects in a crystalline surface cause a local region of disorder in the otherwise ordered surface. A schematic example of a sulphur vacancy in  $\text{MoS}_2$  is shown in figure 1 (a). The defect contributes to a reduction in the intensity of helium flux that is scattered into the Bragg diffraction channels, instead scattering the signal into a broad background. The method can therefore be interpreted as a purely geometric quantification of the degree of order in a surface making the technique agnostic to a sample's chemical or optical properties.

An increasing defect density,  $\Theta$ , will therefore result in a decreasing intensity within the diffraction peaks. The relationship is fully captured by the lattice gas equation,

$$\frac{I}{I_0} = (1 - \Theta)^{\frac{\sigma}{n}} \quad (1)$$

where  $\Theta$  is the defect density expressed as a fraction of the available sites on the surface,  $\sigma$  is the cross section and  $n$  is the unit cell area [18]. It is important to notice that, for a given defect density ( $\Theta$ ) the differential intensity is solely dependent on the ratio of the defect scattering cross-section ( $\sigma$ ) to the, also fixed, unit cell area ( $n$ ),  $\sigma/n$ . The enhanced scattering cross-section, that is unique to atomic helium, is therefore key in achieving high sensitivity to even relatively low defect densities. This relationship also highlights that the method can be applied, without adjustment to theory or experiment, to any other 2D material with vacancy-type defects. We present complimentary calculations in the Methods section that use a toy He-surface interaction potential (figure S3.1), including interpolated site and defect interaction potentials determined from DFT, to demonstrate that increasing disorder in the surface yields a lowering of the proportion of ordered Bragg diffraction and an increase in disorder, cosine-like diffuse scattering (figure S6).

By reference to the intensity from a pristine sample,  $I_0$ , the defect density can therefore be inferred from diffraction intensity,  $I$ . We note that equation 1 holds for discrete defects of the same type and may break down for very high defect densities where nearby defects can interact, or where the number of double vacancies becomes non-negligible. Under this consideration, TMDs such as MoS<sub>2</sub> represent the most extreme test case of our method because they have a very high defect density ( $10^{13} - 10^{15} \text{cm}^{-2}$ )[6], [26] compared to other 2D materials commonly used in optoelectronics, e.g. graphene or hBN have densities between  $10^9 - 10^{13} \text{cm}^{-2}$  depending on fabrication method[27], [28]. The helium scattering cross section  $\sigma$  is not directly related to the physical size of the defect due to long-range interactions between the defect and the helium atom[18]. However, it is possible to computationally calculate the cross section by simulating the diffraction of helium from the defective surface.

## Measuring vacancy-type defect density in ML- MoS<sub>2</sub>

Three ML- MoS<sub>2</sub> samples of different defect density were prepared by mechanical exfoliation and placed on a  $\sim 25 \text{nm}$  thick hBN buffer which in turn sits upon a SiO<sub>2</sub>/Si substrate. The hBN protects the morphological and electronic properties of the ML- MoS<sub>2</sub>, as previously shown using LEEM/D and PL[29]. In figure 2 (a) we show that a similar protective effect is observed with HAMD. Optical and helium atom images of the native defect density sample are shown in figure 2 (b,c).

The first sample had the native defect density while the second and third samples were annealed under Ar/H<sub>2</sub> atmosphere to induce higher level of defects. Full sample details are recorded in Table S2 of the Methods/Sample preparation section. We precisely induce S-vacancy defects in ML-MoS<sub>2</sub> using the annealing procedure first demonstrated by Zhu et al.[6]. To ensure fine control of defect density in our samples we have used the same annealing parameters as used in the original work by Zhu et al. [6] which are calibrated against synchrotron XPS and low-temperature PL. Further information, including annealing parameters, is available in the Methods section.

2D atom micro-diffraction patterns for the first ( $0.1 \times 10^{14} \text{cm}^{-2}$ ) and third ( $1.8 \times 10^{14} \text{cm}^{-2}$ )[6] samples are shown in figure 3, with the intensity scales normalised. All diffraction measurements presented were acquired at a sample temperature of 200°C after initial *in-situ* annealing at 220°C for 2 hours. 2H- MoS<sub>2</sub> is stable, under inert/vacuum atmosphere up to  $\sim 750 \text{K}$  [30]. Diffraction data is acquired at an elevated temperature to ensure the cleanliness of the sample surface from adsorbates. Temperature dependence of diffraction measurements ranging from 220-40°C is

presented in *Supplementary Information (figures S2, S3)* sections and demonstrates that the measurement of defect density is independent of sample temperature within the thermal limits of the material. The plots show the parallel momentum transfer (labelled  $\Delta K$ ) radially, with the orientation of the crystal surface (labelled  $\alpha$ ) plotted azimuthally, the patterns can be considered a representation of the reciprocal surface lattice. The trigonal sulphur surface lattice is clearly seen, and the spacing of diffraction peaks matches expected sulphur-sulphur spacing on the surface of the ML-MoS<sub>2</sub>:  $3.20 \pm 0.07 \text{ \AA}$  measured compared to  $\sim 3.15 \text{ \AA}$  in literature[31]. Details of lattice constant measurement are shown in figure S1. Comparing the two patterns we observe a significant decrease in intensity of diffraction peaks whilst the peak positions remain unchanged, thus qualitatively confirming the sensitivity of HAMD disruptions in long-range electronic order caused by atomic vacancies.

The electronic order of the surface is, broadly speaking, sensitive to three parameters that describe a potential energy surface (PES),

- i) level of corrugation, which usually increases the difference between minima and maxima in a PES,
- ii) lattice constant,
- iii) degree of order, or lattice regularity.

The corrugation (i) and lattice constant (ii) are primarily responsible for changing relative diffraction peak intensities and their positions in  $\Delta K$ , respectively. As such, changes in absolute diffracted intensity, as seen in figure 3, are attributed to changing defect density ( $\theta$ ) (iii) and can therefore be modelled using equation 1. Further discussion on PES is presented in the Methods/Modelling section.

1-dimensional diffraction scans were taken along the principal azimuth ( $\langle 10 \rangle$  direction) for each sample, e.g. line-cut at  $\alpha = 30^\circ$  in figure 3, shown in figure 4 (a). The measurements were normalised using a diffusely scattered background measured on the SiO<sub>2</sub> substrate to account for fluctuations in detection sensitivity. We extract the diffracted helium intensity by Gaussian fitting of the (-1,0) and (-2,0) peaks. The relationship of intensity to defect density of (-2,0) is shown in figure 4 (b), and the (-1,0) equivalent shown in Supplementary Information section S5, figure S4. The (0,0) (specular) and (-3,0) peaks are not used here due to their high sensitivity to sample tilt and low intensity, respectively, although in principle the method works for any diffraction condition, including those with out-of-plane momentum transfer.

Fitting the lattice gas model (equation 1) to the (-2,0) peak yields a helium-defect cross-section of  $35.8 \pm 5.3 \text{ \AA}^2$  and  $35.3 \pm 2.8 \text{ \AA}^2$  for (-1,0). These cross-sections are empirically determined and do not rely on the supporting computational work described in Methods. Values are not necessarily expected to be the same for every diffraction peak [18]. An important result is that the cross sections are significantly larger than the area of a unit cell,  $8.6 \text{ \AA}^2$ , highlighting the sensitivity of our approach. The enlarged cross section means that for defect densities larger than  $\sim 2 \times 10^{14} \text{ cm}^{-2}$  our assumption of mostly isolated single defects will break down and a more complex model is needed where defect cross-sections are permitted a degree of overlap. This situation is, however, rare because the morphological ordering, which is a less direct and sensitive predictor of optoelectronic properties than long-range electronic order, of TMDs is found to completely degrade in the  $10^{14} \text{ cm}^{-2}$  defect density range[2]. We also note that our cross sections are somewhat smaller than helium-adatom cross sections found in the literature, which can be explained by the increased volume of space affected by the long-range attractive part of the potential for adsorbed adatoms compared to vacancies.

The fitted model shown in figure 4 (b) acts as a calibration curve for all ML- MoS<sub>2</sub> where the scattering geometry from figure 1 (a) because it is solely dependent on the He-defect scattering cross-section,  $\theta$ . With a one-time calibration of a given material against a stoichiometric technique like beamline XPS, one can repeatedly perform measurements of vacancy-type defect density.

One can look towards high-throughput quality control of 2D semiconductors by integrating HAMD into molecular beam epitaxy (MBE) or chemical vapour deposition (CVD) systems directly as an *in-situ* measurement of defect density immediately after wafer growth. Owing to its non-destructive, chemically inert beam and ability to measure intrinsic, unprepared semiconductors, the wafers would be unaffected by the measurement and can go on to be used in further manufacturing steps. The key innovations, in instrumentation, that enable the few-micron spot size in the current work are recent advances in the generation of intense neutral atom sources [32], [33] and custom high-sensitivity atom detectors [23]. Favourable scaling of the detected helium intensity ( $I$ ) with beam spot-size ( $r$ ),  $I \propto 1/r^4$  [34], means that scaling our method to commercial viability is not only simple but cost effective because the current implementation represents the cutting-edge of modern instrumentation. With increased signal one can perform detection with a generic mass spectrometer and both decrease measurements times and improve accuracy, as both are ultimately determined by the achievable signal-to-noise ratio.

## Conclusion

We have demonstrated helium atom micro-diffraction (HAMD) as a direct and non-destructive method for the measurement of vacancy-type defect density in device-scale ( $\sim 15 \times 20 \mu\text{m}$ ) monolayer TMDs using the prototypical MoS<sub>2</sub>. We think that HAMD will become an indispensable tool for the characterisation of defect density in 2D materials spanning the microscopic and wafer scales to support the ever-growing academic and industrial research and development of 2D material-based devices.

We present a simple quantitative model, the lattice gas equation, that accurately captures the relationship between Bragg intensity and vacancy-type defect density in monolayer MoS<sub>2</sub>. We also performed *ab initio* calculations that show, together with the lattice gas model, that the method's contrast is independent of surface chemistry or structure. This allows it to be applied immediately to a wide range of systems whose optoelectronic, mechanical or thermal properties can be modulated *via* surface defects or dopants, examples include hBN[35], graphene[36], doped diamond[37], alongside other TMDs.

We have leveraged recent advances in neutral atom beam generation and detection to demonstrate the most challenging implementation of the method by performing it with microscopic spatial resolution ( $5 \mu\text{m}$  beam spot size). We outline how, due to favourable scaling between beam spot size and detected signal, the method is highly scalable and immediately integrable into wafer growth systems (e.g. MBE and CVD), enabling *in-situ* quality control that is critical for the widespread adoption of 2D materials in devices.

Future work could leverage the technique's demonstrated sensitivity to surface electronic structure to investigate a range properties that also have significant effects on device performance and are encoded within atomic Bragg scattering, such as surface contamination, thermal expansion coefficients and electron-phonon coupling in monolayer materials[38], [39], [40], [41], with accessible characterisation areas spanning microns to centimetres.

## Main Figures:

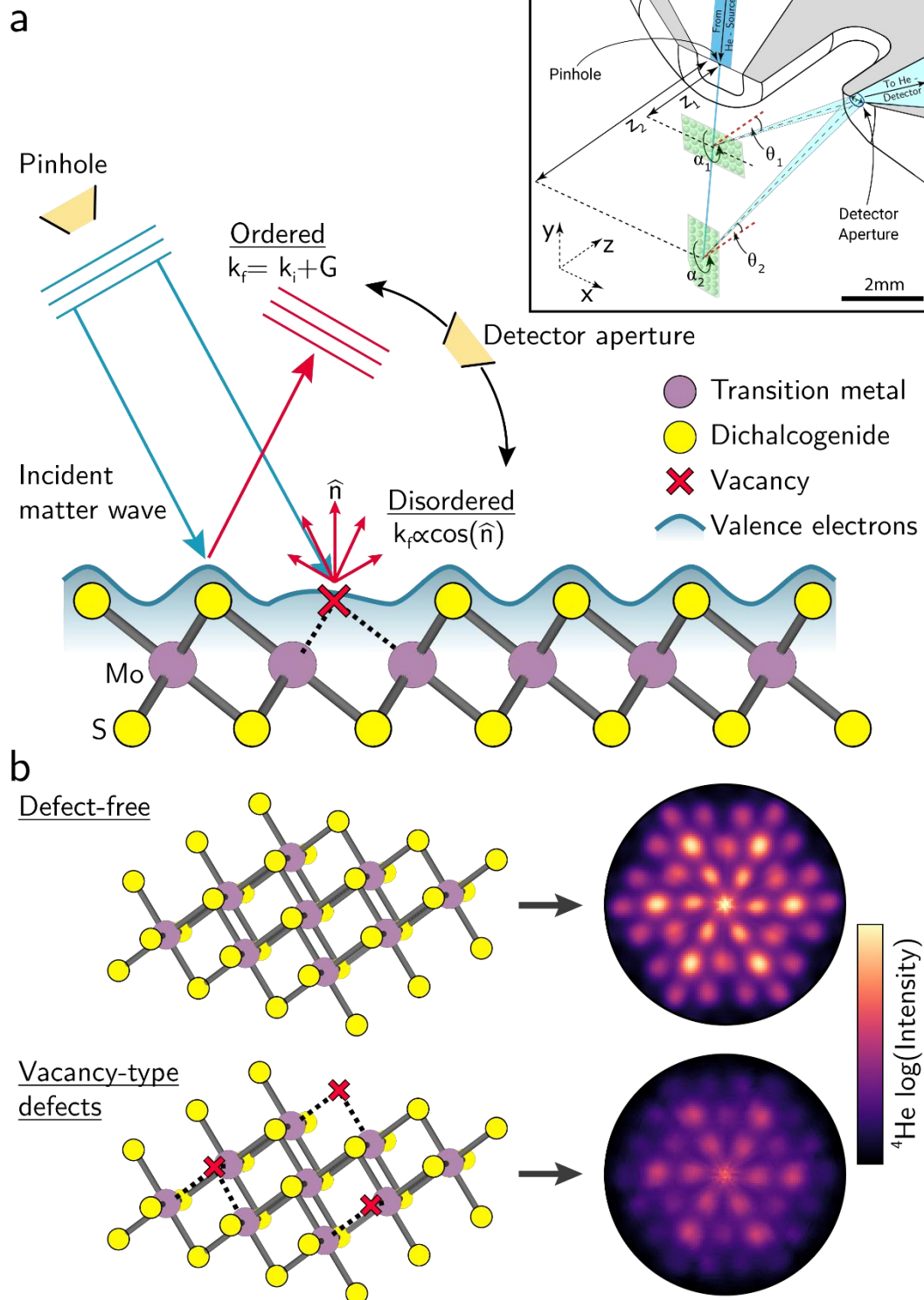


**Figure 1 – An overview of helium atom micro-diffraction:** (a) Schematic of helium atom micro-diffraction (HAMD) scattering from the outermost electron density of a TMD surface with vacancy-type defects shown as red crosses. Different diffraction conditions are measured by changing the angle of detection of the atom detector, the inset from von Jeinsen et al.[16] shows a diagram of the sample environment used. The competing contrast mechanisms, Bragg (ordered) and diffuse (disordered) scattering, are shown in red. Both are collected at the detector aperture and their ratio encodes the long-range electronic order, and therefore defect density, at the material's surface. We show typical HAMD data from a highly ordered (low defect density) surface (b), and the equivalent data for a less ordered (higher defect density) surface (c), using real data presented in full in figure 3. Inset reproduced with permission from von Jeinsen et al.[21].



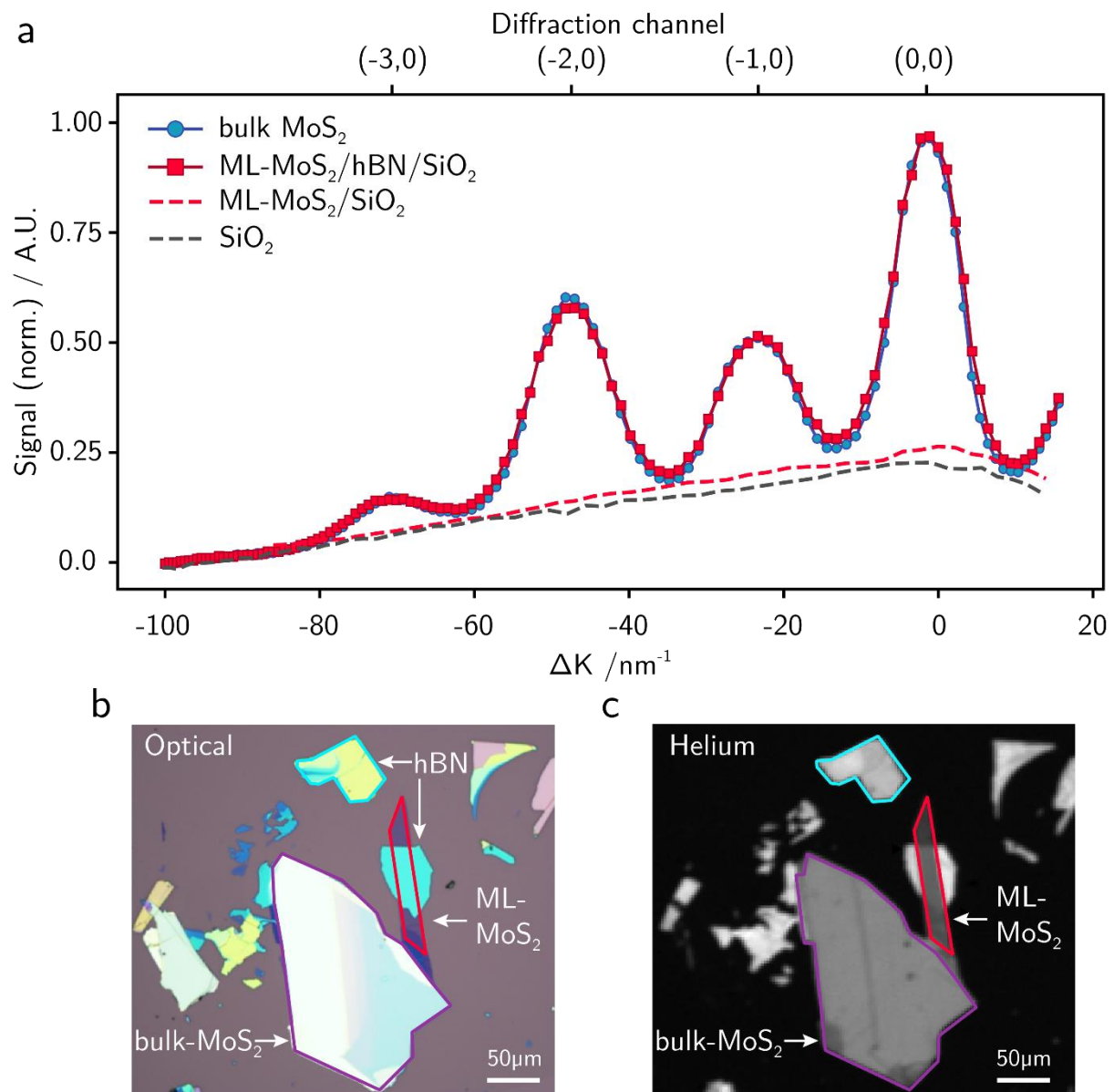


**Figure 2 – Preserving long-range electronic order in ML-MoS<sub>2</sub> using hBN:** (a) 1-dimensional diffraction scans of  $\text{SiO}_2$ , bulk  $\text{MoS}_2/\text{SiO}_2$ , ML- $\text{MoS}_2/\text{SiO}_2$  and ML- $\text{MoS}_2/\text{hBN}/\text{SiO}_2$  acquired along the materials' principal azimuths. Here, all  $\text{MoS}_2$  measured has the native ( $0.1 \times 10^{14} \text{cm}^{-2}$ ) defect density. It is interesting to note that diffraction from the bulk and ML- $\text{MoS}_2$  is very similar, implying the same for their long-range electronic ordering. Optical (b) and helium atom (c) images show the regions measured in (a).



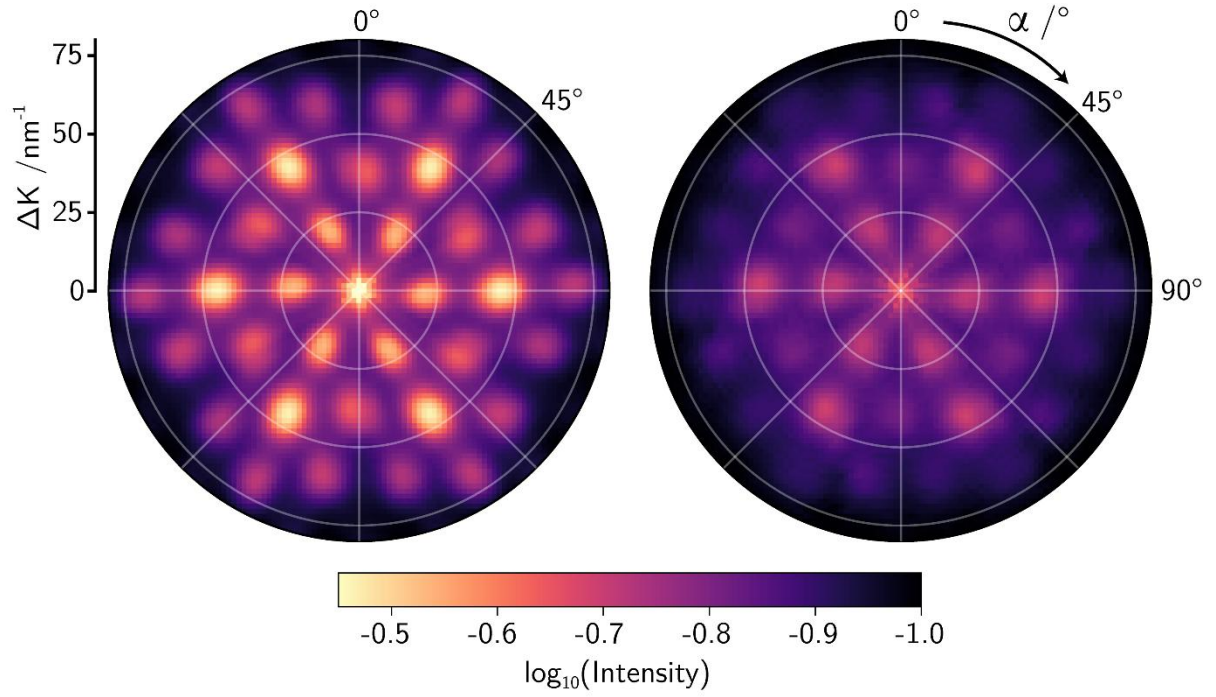


**Figure 3 – The effect of defects on helium atom micro-diffraction:** 2D diffraction scan of lowest (left) and highest (right) defect densities of monolayer MoS<sub>2</sub> measured in this study. The native defect density ( $0.1 \times 10^{14} \text{ cm}^{-2}$ , left) produces more intense diffraction peaks at all orders in comparison to the most defective sample ( $1.8 \times 10^{14} \text{ cm}^{-2}$ , right). The positions of the diffraction peaks remain the same. Both plots are normalized to the maximum value in the native defect density (specular condition at  $\Delta K = 0 \text{ nm}^{-1}$ ). 2D diffraction data acquired as a 70° section, from  $\alpha = (0, 70)^\circ$ , to ensure full coverage of the Brillouin zone. The data is then tiled to cover all values of azimuthal rotation,  $\alpha$ .

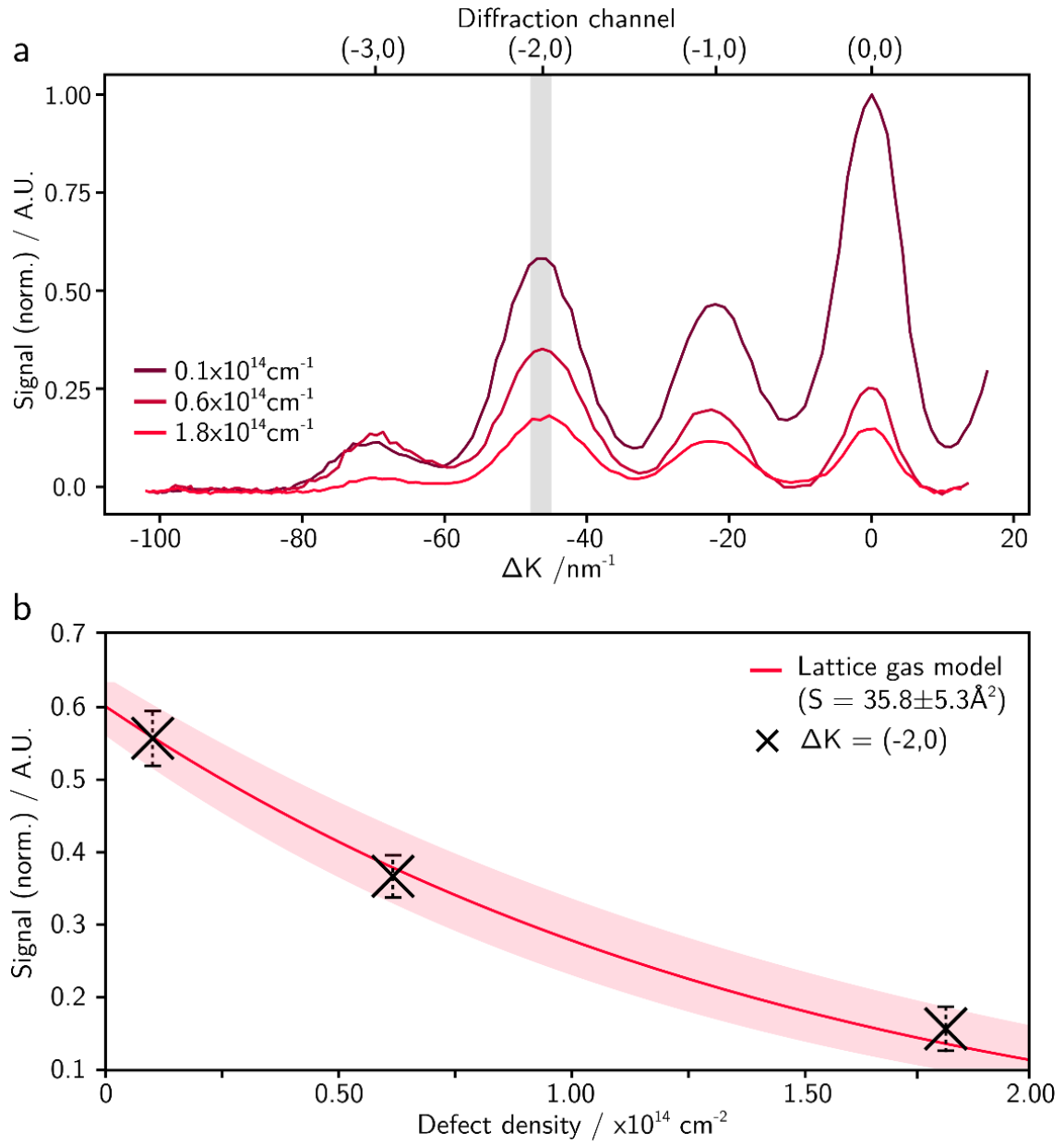


**Figure 4 – Quantifying defect density in ML-MoS<sub>2</sub>:** Panel (a), line scans of increasing defect density monolayer MoS<sub>2</sub> acquired at 200°C showing a consistent decrease in diffracted intensity as defect density increases. Panel (b) shows intensities extracted using Gaussian fitting to the (-2,0) diffraction peaks and excellent agreement with the lattice gas model from equation 1.

## Bibliography

- [1] E. C. Regan *et al.*, 'Emerging exciton physics in transition metal dichalcogenide heterobilayers', *Nat Rev Mater*, vol. 7, no. 10, pp. 778–795, Oct. 2022, doi: 10.1038/s41578-022-00440-1.
- [2] J. Yang *et al.*, 'Single Atomic Vacancy Catalysis', *ACS Nano*, vol. 13, no. 9, pp. 9958–9964, Sep. 2019, doi: 10.1021/acsnano.9b05226.
- [3] E. Mitterreiter *et al.*, 'The role of chalcogen vacancies for atomic defect emission in MoS<sub>2</sub>', *Nat Commun*, vol. 12, no. 1, p. 3822, Jun. 2021, doi: 10.1038/s41467-021-24102-y.
- [4] K. Barthelmi *et al.*, 'Atomistic defects as single-photon emitters in atomically thin MoS<sub>2</sub>', *Appl Phys Lett*, vol. 117, no. 7, p. 70501, Aug. 2020, doi: 10.1063/5.0018557.
- [5] C. Chakraborty, N. Vamivakas, and D. Englund, 'Advances in quantum light emission from 2D materials', *Nanophotonics*, vol. 8, Aug. 2019, doi: 10.1515/nanoph-2019-0140.
- [6] Y. Zhu *et al.*, 'Room-Temperature Photoluminescence Mediated by Sulfur Vacancies in 2D Molybdenum Disulfide', *ACS Nano*, vol. 17, no. 14, pp. 13545–13553, Jul. 2023, doi: 10.1021/acsnano.3c02103.
- [7] K. Xu *et al.*, 'Validating the Use of Conductive Atomic Force Microscopy for Defect Quantification in 2D Materials', *ACS Nano*, vol. 17, no. 24, pp. 24743–24752, 2023, doi: 10.1021/acsnano.3c05056.
- [8] O. Lopez-Sanchez, D. Lembke, M. Kayci, A. Radenovic, and A. Kis, 'Ultrasensitive photodetectors based on monolayer MoS<sub>2</sub>', *Nat Nanotechnol*, vol. 8, no. 7, pp. 497–501, Jul. 2013, doi: 10.1038/nnano.2013.100.
- [9] M. Bergin, D. J. Ward, J. Ellis, and A. P. Jardine, 'A method for constrained optimisation of the design of a scanning helium microscope', *Ultramicroscopy*, vol. 207, p. 112833, 2019, doi: <https://doi.org/10.1016/j.ultramic.2019.112833>.
- [10] B. Holst *et al.*, 'Material properties particularly suited to be measured with helium scattering: selected examples from 2D materials, van der Waals heterostructures, glassy materials, catalytic substrates, topological insulators and superconducting radio frequency materials', *Phys. Chem. Chem. Phys.*, vol. 23, no. 13, pp. 7653–7672, 2021, doi: 10.1039/D0CP05833E.
- [11] M. Barr *et al.*, 'A design for a pinhole scanning helium microscope', *Nucl Instrum Methods Phys Res B*, vol. 340, pp. 76–80, Dec. 2014, doi: 10.1016/j.nimb.2014.06.028.
- [12] M. Koch *et al.*, 'Imaging with neutral atoms—a new matter-wave microscope', *J Microsc*, vol. 229, no. 1, pp. 1–5, 2008, doi: <https://doi.org/10.1111/j.1365-2818.2007.01874.x>.
- [13] T.A. Myles, S.D. Eder, M.G. Barr, A. Fahy, J. Martes, and P.C. Dastoor, 'Taxonomy through the lens of neutral helium microscopy', *Scientific Reports* 2019 9:1, vol. 9, no. 1, pp. 1–10, Feb. 2019, doi: 10.1038/s41598-018-36373-5.
- [14] S. M. Lambrick *et al.*, 'Multiple scattering in scanning helium microscopy', *Appl Phys Lett*, vol. 116, no. 6, p. 61601, Feb. 2020, doi: 10.1063/1.5143950.

- [15] G. Bhardwaj, K. R. Sahoo, R. Sharma, P. Nath, and P. R. Shirhatti, 'Neutral-atom-scattering-based mapping of atomically thin layers', *Phys Rev A (Coll Park)*, vol. 105, no. 2, p. 22828, Feb. 2022, doi: 10.1103/PhysRevA.105.022828.
- [16] A. Radić, S. M. Lambrick, N. A. von Jeinsen, A. P. Jardine, and D. J. Ward, '3D surface profilometry using neutral helium atoms', *Appl Phys Lett*, vol. 124, no. 20, p. 204101, May 2024, doi: 10.1063/5.0206374.
- [17] A. Radić *et al.*, 'Heliometric stereo: a new frontier in surface profilometry', Jan. 2025, Accessed: Jun. 25, 2025. [Online]. Available: <https://arxiv.org/abs/2501.14833v1>
- [18] B. Poelsema and G. Comsa, *Scattering of Thermal Energy Atoms, from Disordered Surfaces*, 1st ed. Springer, 1989. [Online]. Available: <https://doi.org/10.1007/BFb0045229>
- [19] D. Farías and K. H. Rieder, 'Atomic beam diffraction from solid surfaces', *Rep. Prog. Phys.*, vol. 61, no. 12, pp. 1575–1664, 1998.
- [20] P. Witham and E. Sánchez, 'A simple approach to neutral atom microscopy', *Review of Scientific Instruments*, vol. 82, no. 10, p. 103705, Oct. 2011, doi: 10.1063/1.3650719.
- [21] N. A. von Jeinsen *et al.*, '2D Helium Atom Diffraction from a Microscopic Spot', *Phys Rev Lett*, vol. 131, no. 23, p. 236202, Dec. 2023, doi: 10.1103/PhysRevLett.131.236202.
- [22] C. J. Hatchwell, M. Bergin, B. Carr, M. G. Barr, A. Fahy, and P. C. Dastoor, 'Measuring scattering distributions in scanning helium microscopy', *Ultramicroscopy*, vol. 260, p. 113951, Jun. 2024, doi: 10.1016/j.ultramic.2024.113951.
- [23] M. Bergin *et al.*, 'Low-energy electron ionization mass spectrometer for efficient detection of low mass species', *Review of Scientific Instruments*, vol. 92, no. 7, p. 73305, Jul. 2021, doi: 10.1063/5.0050292.
- [24] M. Bergin, S. M. Lambrick, H. Sleath, D. J. Ward, J. Ellis, and A. P. Jardine, 'Observation of diffraction contrast in scanning helium microscopy', *Sci Rep*, vol. 10, no. 1, pp. 1–8, Feb. 2020, doi: 10.1038/s41598-020-58704-1.
- [25] S. M. Lambrick *et al.*, 'Observation of diffuse scattering in scanning helium microscopy', *Phys. Chem. Chem. Phys.*, vol. 24, no. 43, pp. 26539–26546, 2022, doi: 10.1039/D2CP01951E.
- [26] X. Zhang *et al.*, 'Low-Defect-Density Monolayer MoS<sub>2</sub> Wafer by Oxygen-Assisted Growth-Repair Strategy', *Advanced Science*, vol. 11, no. 42, p. 2408640, Nov. 2024, doi: 10.1002/ADVS.202408640.
- [27] D. Edelberg *et al.*, 'Approaching the Intrinsic Limit in Transition Metal Diselenides via Point Defect Control', *Nano Lett*, vol. 19, no. 7, pp. 4371–4379, Jul. 2019, doi: 10.1021/ACS.NANOLETT.9B00985/ASSET/IMAGES/MEDIUM/NL-2019-009856\_M003.GIF.
- [28] R. Gong *et al.*, 'Coherent dynamics of strongly interacting electronic spin defects in hexagonal boron nitride', *Nature Communications* 2023 14:1, vol. 14, no. 1, pp. 1–10, Jun. 2023, doi: 10.1038/s41467-023-39115-y.
- [29] M. K. L. Man *et al.*, 'Protecting the properties of monolayer MoS<sub>2</sub> on silicon based substrates with an atomically thin buffer', *Scientific Reports* 2016 6:1, vol. 6, no. 1, pp. 1–9, Feb. 2016, doi: 10.1038/srep20890.

- [30] F. Loi *et al.*, 'Growth Mechanism and Thermal Stability of a MoS<sub>2</sub>-Graphene Interface: A High-Resolution Core-Level Photoelectron Spectroscopy Study', *Journal of Physical Chemistry C*, vol. 124, no. 38, pp. 20889–20897, Sep. 2020, doi: 10.1021/ACS.JPCC.0C05037/ASSET/IMAGES/LARGE/JP0C05037\_0007.JPEG.
- [31] T. M. N. Nguyen, V.-D. Vuong, M. T. Phong, and T. Van Le, 'Fabrication of MoS<sub>2</sub> Nanoflakes Supported on Carbon Nanotubes for High Performance Anode in Lithium-Ion Batteries (LIBs)', *J Nanomater*, vol. 2019, no. 1, p. 8364740, 2019, doi: 10.1155/2019/8364740.
- [32] J. Kelsall, A. Radić, J. Ellis, D. J. Ward, and A. P. Jardine, 'Minimizing interference in low-pressure supersonic beam sources', *Journal of Chemical Physics*, vol. 162, no. 9, p. 94304, Mar. 2025, doi: 10.1063/5.0247870/3338235.
- [33] A. Radić, S. M. Lambrick, S. Rhodes, and D. J. Ward, 'On the application of components manufactured with stereolithographic 3D printing in high vacuum systems', *Vacuum*, vol. 232, p. 113809, Feb. 2025, doi: 10.1016/j.vacuum.2024.113809.
- [34] M. Bergin, D. J. Ward, J. Ellis, and A. P. Jardine, 'A method for constrained optimisation of the design of a scanning helium microscope', p. 112833, doi: 10.1016/j.ultramic.2019.112833.
- [35] H. L. Stern *et al.*, 'A quantum coherent spin in hexagonal boron nitride at ambient conditions', *Nat Mater*, May 2024, doi: 10.1038/s41563-024-01887-z.
- [36] M. D. Bhatt, H. Kim, and G. Kim, 'Various defects in graphene: a review', *RSC Adv*, vol. 12, no. 33, pp. 21520–21547, 2022, doi: 10.1039/d2ra01436j.
- [37] Y. Einaga, 'Boron-Doped Diamond Electrodes: Fundamentals for Electrochemical Applications', *Acc Chem Res*, vol. 55, no. 24, pp. 3605–3615, Dec. 2022, doi: 10.1021/acs.accounts.2c00597.
- [38] G. Anemone, A. Al Taleb, A. Castellanos-Gomez, and D. Farías, 'Experimental determination of thermal expansion of natural MoS<sub>2</sub>', *2d Mater*, vol. 5, no. 3, p. 35015, May 2018, doi: 10.1088/2053-1583/aabe4a.
- [39] G. Anemone, A. Al Taleb, G. Benedek, A. Castellanos-Gomez, and D. Farías, 'Electron-Phonon Coupling Constant of 2H-MoS<sub>2</sub>(0001) from Helium-Atom Scattering', *Journal of Physics Chemistry C*, vol. 123, no. 6, pp. 3682–3686, 2019, doi: 10.1021/acs.jpcc.8b12029.
- [40] A. Al Taleb, G. Anemone, R. Miranda, and D. Farías, 'Characterization of interlayer forces in 2D heterostructures using neutral atom scattering', *2d Mater*, vol. 5, no. 4, p. 45002, Jul. 2018, doi: 10.1088/2053-1583/aacf26.
- [41] N. von Jeinsen *et al.*, 'Helium atom micro-diffraction as a characterisation tool for 2D materials', *ArXiv*, Sep. 2024, [Online]. Available: <https://arxiv.org/abs/2409.20461>
- [42] K. F. Mak, C. Lee, J. Hone, J. Shan, and T. F. Heinz, 'Atomically thin MoS<sub>2</sub>: A new direct-gap semiconductor', *Phys Rev Lett*, vol. 105, no. 13, p. 136805, Sep. 2010, doi: 10.1103/PHYSREVLETT.105.136805/MOS2\_SUPPLEMENT\_PRL\_1AUG10.DOC.
- [43] S. Paul, R. Torsi, J. A. Robinson, and K. Momeni, 'Effect of the Substrate on MoS<sub>2</sub> Monolayer Morphology: An Integrated Computational and Experimental Study', *ACS Appl*

- Mater Interfaces*, vol. 14, no. 16, pp. 18835–18844, Apr. 2022, doi: 10.1021/ACSAMI.2C03471.
- [44] W. Jin *et al.*, ‘Substrate interactions with suspended and supported monolayer MoS<sub>2</sub>: Angle-resolved photoemission spectroscopy’, *Phys Rev B Condens Matter Mater Phys*, vol. 91, no. 12, p. 121409, Mar. 2015, doi: 10.1103/PHYSREVB.91.121409/SUPPLEMENTAL\_MATERIAL.PDF.
  - [45] J. H. Lambert, ‘Photometria Sive De Mensura Et Gradibus Luminis, Colorum Et Umbrae’, 1760, *Klett Augustae Vindelicorum, Augustae Vindelicorum*.
  - [46] E. Gnecco *et al.*, ‘Atomic-scale characterization of contact interfaces between thermally self-assembled Au islands and few-layer MoS<sub>2</sub> surfaces on SiO<sub>2</sub>’, *Appl Surf Sci*, vol. 616, p. 156483, Apr. 2023, doi: 10.1016/j.apsusc.2023.156483.
  - [47] N. A. von Jeinsen, ‘Leveraging Spatial and Angular Resolution in Scanning Helium Microscopy to Study Technological Samples’, University of Cambridge, 2021.
  - [48] S. M. Lambrick, M. Bergin, A. P. Jardine, and D. J. Ward, ‘A ray tracing method for predicting contrast in neutral atom beam imaging’, *Micron*, vol. 113, pp. 61–68, Oct. 2018, doi: 10.1016/j.micron.2018.06.014.
  - [49] A. Fahy, M. Barr, J. Martens, and P. C. Dastoor, ‘A highly contrasting scanning helium microscope’, *Review of Scientific Instruments*, vol. 86, no. 2, p. 23704, Feb. 2015, doi: 10.1063/1.4907539.
  - [50] D. E. Manolopoulos, R. E. Wyatt, and D. C. Clary, ‘Iterative solution in quantum scattering theory. The log derivative Kohn approach’, vol. 86, no. 10, pp. 1641–1648, doi: 10.1039/FT9908601641.
  - [51] G. Wolken, ‘Collision of a diatomic molecule with a solid surface’, *J Chem Phys*, vol. 59, no. 3, pp. 1159–1165, Aug. 1973, doi: 10.1063/1.1680162.
  - [52] S. Lambrick, D. Seremet, and S. Lambrick, ‘slambrick/SHeM-Ray-Tracing-Simulation: 2D helium atom diffraction from a microscopic spot Latest Edit: 2D helium atom diffraction from a microscopic spot Delete: 2D helium atom diffraction from a microscopic spot (final version)’, doi: 10.5281/ZENODO.8096928.
  - [53] S. J. Clark *et al.*, ‘First principles methods using CASTEP’, *Zeitschrift fur Kristallographie*, vol. 220, no. 5–6, pp. 567–570, May 2005, doi: 10.1524/ZKRI.220.5.567.65075/MACHINEREADABLECITATION/RIS.
  - [54] J. P. Perdew, K. Burke, and M. Ernzerhof, ‘Generalized Gradient Approximation Made Simple’, *Phys Rev Lett*, vol. 77, no. 18, p. 3865, Oct. 1996, doi: 10.1103/PhysRevLett.77.3865.
  - [55] J. Moellmann and S. Grimme, ‘DFT-D3 study of some molecular crystals’, *Journal of Physical Chemistry C*, vol. 118, no. 14, pp. 7615–7621, Apr. 2014, doi: 10.1021/JP501237C/SUPPL\_FILE/JP501237C\_SI\_001.PDF.
  - [56] D. Vanderbilt, ‘Soft self-consistent pseudopotentials in a generalized eigenvalue formalism’, *Phys Rev B*, vol. 41, no. 11, p. 7892, Apr. 1990, doi: 10.1103/PhysRevB.41.7892.



- [57] H. J. Monkhorst and J. D. Pack, 'Special points for Brillouin-zone integrations', *Phys Rev B*, vol. 13, no. 12, p. 5188, Jun. 1976, doi: 10.1103/PhysRevB.13.5188.
- [58] J. R. Manson, G. Benedek, and S. Miret-Artés, 'Atom scattering as a probe of the surface electron-phonon interaction at conducting surfaces', *Surf Sci Rep*, vol. 77, no. 2, p. 100552, May 2022, doi: 10.1016/j.surfrep.2022.100552.

## Data Availability:

The data underlying all figures in the main text and Supplementary Information will be made publicly available from the University of Cambridge repository upon publication.

## Code Availability:

All code used in this work is available from the corresponding authors upon reasonable request.

## Acknowledgements:

The work was supported by EPSRC grant EP/R008272/1, Innovate UK/Ionoptika Ltd. through Knowledge Transfer Partnership 10000925. The work was performed in part at CORDE, the Collaborative R&D Environment established to provide access to physics related facilities at the Cavendish Laboratory, University of Cambridge and EPSRC award EP/T00634X/1. S.M.L. acknowledges support from EPSRC grant EP/X525686/1. K.W. and T.T. acknowledge support from the JSPS KAKENHI (Grant Numbers 21H05233 and 23H02052), the CREST (JPMJCR24A5), JST and World Premier International Research Center Initiative (WPI), MEXT, Japan. The authors thank Christoph Schnedermann for useful discussions.

## Supplementary materials

Materials and methods (experimental)

Methods (computational)

Tables S1-S4

Figures S1-S6

# Supplementary Materials for

# Measuring vacancy-type defect density in monolayer MoS<sub>2</sub>

Aleksandar Radić\*, Nick von Jeinsen, Vivian Perez, Ke Wang, Min Lin, Boyao Liu, Yiru Zhu, Ismail Sami, Kenji Watanabe, Takashi Taniguchi, David Ward, Andrew Jardine, Akshay Rao, Manish Chhowalla\*, Sam Lambrick\*

\*Author emails: [ar2071@cam.ac.uk](mailto:ar2071@cam.ac.uk), [mc209@cam.ac.uk](mailto:mc209@cam.ac.uk), [sml59@cantab.ac.uk](mailto:sml59@cantab.ac.uk)

## **This PDF file includes:**

Materials and methods (experimental)

Methods (computational)

Tables S1-S4

Figures S1-S6

## S1 – Comparing defect density measurement techniques

Table S1 provides a non-exhaustive comparison of the key characteristic and limits of the current standard techniques for vacancy-type defect density measurement (XPS = x-ray photoelectron spectroscopy, PL = photoluminescence, cAFM = conductive atomic force microscopy, STM = scanning tunnelling microscopy, (S)TEM = (scanning) transmission electron microscopy).

Technique (model)	Days /per sample	Lab-based?	Destructive?	Sample requirements/prep.	Lateral resolution	Access time	Direct measure of defect density (Y/N)
Beamline XPS (Diamond Light Source – I06, I09, B07)	N/A	No	Yes	X, ultrahigh vacuum	4 × 20µm	months	Yes
Lab XPS (ThermoFisher Nexsa G2)	2	Yes	Mode/material dependent	X, ultrahigh vacuum	10 – 400µm	weeks	Yes
Low temp. PL (Horiba Scientific)	0.25	Yes	Material dependent	Optically transparent, low PL substrates	~1µm	weeks	No
cAFM (Veeco Dimension Pro)	2	Yes	Mode /material dependent	Conductive, high vacuum	<1nm	weeks	Yes – statistical extrapolation
STM	2	Yes	Mode/material dependent	Conductive, high vacuum	<1nm	weeks	Yes – statistical extrapolation
(S)TEM (FEI Tecnai G2)	2	Yes	Yes	Conductive/conductive coating, ultrahigh vacuum	<1nm	weeks/months	Yes – statistical extrapolation
Helium atom micro-diffraction	1	Yes	No	High vacuum	5µm (350nm achieved in literature)	weeks	Yes

**Table S1 - Standard defect density characterization techniques compared with helium atom micro-diffraction:** A non-exhaustive list of standard characterisation techniques used to measure vacancy-type defect density in ML-TMDs. Time taken per sample includes estimates of typical sample preparation, measurement time and data analysis. Time to access refers to the typical availability of a given technique at the University of Cambridge, including research proposal submission/consideration if applicable. Costs for lab XPS, photoluminescence and helium atom micro-diffraction are taken as the full service mode rate for internal users as determined by the collaborative R&D environment for physics at the Cavendish Laboratory ([CORDE](#)). Costs for cAFM and TEM taken as full service mode rate for internal users as determined by the [Cambridge Centre for Gallium Nitride](#) and [Cambridge Advanced Imaging Centre](#), respectively. In all cases industry rates are higher and access times may be longer.

## S2 - Materials and Methods (experimental)

### S2.1 - Influence of the substrate on long-range electronic order

Many of the unique and interesting properties of 2D materials derive from the reduced dimensionality of those materials compared to ‘traditional’ 3D materials. Therefore, for both use and analysis of these materials isolating single layers without disturbing their properties is key. It is well documented that the substrates on which 2D materials are placed can significantly affect both the morphological and optoelectronic properties of the 2D layer. For example, previous studies have shown that the interaction between the substrate and monolayer TMDs can quench photoluminescence if the sample is placed directly onto Si/SiO<sub>2</sub>[42], [43]. In contrast, when even monolayers of hBN, LaAlO<sub>3</sub> or SrTiO<sub>3</sub> are placed between the Si/SiO<sub>2</sub> and the TMD, the substrate-TMD interaction is effectively screened, and optoelectronic properties are preserved as if the sample was free-standing[29], [44]. As long-range electronic order is the key determinant for any observed signal in helium atom scattering, helium micro-diffraction measurements are sensitive to small changes in that order induced by the substrate. To validate the isolation of the ML- MoS<sub>2</sub> sample from the substrate, two monolayer MoS<sub>2</sub> flakes were prepared by mechanical exfoliation, the first was placed directly onto a standard SiO<sub>2</sub>/Si substrate, and the second onto ~25 nm hBN which in turn sits atop SiO<sub>2</sub>/Si. An exfoliated flake of bulk MoS<sub>2</sub> was also included for reference. The full sample arrangement is shown in Figure 1(b,c). Figure 2 presents helium micro-diffraction measurements taken on the three samples as well as the silicon dioxide substrate. Both the bulk MoS<sub>2</sub> and the monolayer MoS<sub>2</sub>-hBN demonstrate clear diffraction peaks consistent with scattering along the <10> surface azimuth of the MoS<sub>2</sub> lattice, the silicon oxide signal does not show clear signs of order and is consistent with diffuse scattering from a disordered surface[25]. Comparing the measurements of monolayer MoS<sub>2</sub> on hBN on SiO<sub>2</sub> (red), and monolayer MoS<sub>2</sub> on SiO<sub>2</sub> (grey) directly, the long-range electronic order is entirely destroyed when the ML- MoS<sub>2</sub> lies directly on SiO<sub>2</sub>, shown by the total disappearance of Bragg diffraction peaks leaving only disordered scattering. The resultant disordered scattering from a surface with insignificant long-range electronic order follows a cosine-like scattering distribution centred on the surface-normal[24], [25], demonstrated in the cases of ML- MoS<sub>2</sub>/ SiO<sub>2</sub> and SiO<sub>2</sub> in Figure 2 where their respective maxima both occur at the specular condition ( $\Delta K = 0\text{nm}^{-1}$ ), analogous to Lambertian scattering with light[45].

It is also interesting to note that the atomic helium beam shows subtle differences between ML and bulk MoS<sub>2</sub>, shown in Figure 2. We determine the lattice constant ( $\alpha$ ), calculated from the spacing of the diffraction peaks (figure S1), as  $\alpha = 3.20 \pm 0.07\text{\AA}$  at 373K, which corresponds to a 1.3% lattice expansion in the monolayer compared to literature bulk values of  $\alpha = 3.16\text{\AA}$ . It is interesting to note that previous helium atom scattering studies of the surface of bulk 2H-MoS<sub>2</sub>, reported  $\alpha = 3.25\text{\AA}$ , a 3% lattice expansion in the surface layer compared to the bulk, even when measured at only 100K [39]. Although a direct, quantitative comparison cannot be made due to differences in sample size (micron- versus millimetre-scale), preparation and temperature, this result highlights the importance of measuring truly monolayer samples to properly assess a material’s properties, even with the helium atoms exclusively scattering from the valence electrons in both cases.

Our results confirm previously published low-energy electron diffraction/microscopy (LEED/LEEM)[29] and TEM[46] results which demonstrated structural perturbation to monolayer MoS<sub>2</sub> due to an SiO<sub>2</sub> substrate. However, both LEED and TEM inspect the structure based on the ionic core locations, and while they show degradation in the structural order, they cannot see the

complete collapse of electronic order that dictates key optoelectronic properties. In contrast, HAMD is sensitive to the electronic order in the sample, since it is the valence electrons that the beam interacts with exclusively. The implication is that while physical structural order, as measured by TEM or LEED is degraded in monolayer TMDs on strongly interacting substrates like SiO<sub>2</sub>, the long-range electronic order undergoes a near total collapse. This has important implications for device performance, as it is the long-range electronic order that will ultimately control the electronic and optical properties of devices.

## S2.2 - Sample preparation

The native defect density of MoS<sub>2</sub> is reported as  $< \sim 1 \times 10^{13} \text{cm}^{-2}$  whilst the upper limit is  $\sim 1 \times 10^{15} \text{cm}^{-2}$  before the lattice structure breaks down[2]. Three samples of mechanically exfoliated monolayer MoS<sub>2</sub>, with increasing defect densities were prepared using high temperature annealing under a mixed Ar/H<sub>2</sub> (95%/5%) gas flow, as reported by Zhu et al.[6]. To ensure precise knowledge of defect density we reproduce the annealing parameters exactly from the original work by Zhu et al. [6]. Exact sample annealing protocols and defect densities are listed in Table S2.

Sample	Annealing Protocol		Defect Density / $\times 10^{14} \text{cm}^{-2}$
	Time / hrs	Temp. / °C	
1	N/A	N/A	$\sim 0.1$ (native)
2	0.5	550	0.62
3	0.5	600	1.8

**Table S2 – Annealing protocols used to induce S-vacancies in ML-MoS<sub>2</sub>:** Ar/H<sub>2</sub> annealing protocol used to produce each ML- MoS<sub>2</sub> sample with changing S-vacancy defect density, as outlined by Zhu et al.[6].

Samples were stored in a glovebox with argon atmosphere and transferred into a SHeM with no more than 1h exposure to air. Owing to the chemically and electrically inert helium-4 probe sample preparation prior to insertion into the SHeM is minimal. The SiO<sub>2</sub>/Si substrate, onto which the MoS<sub>2</sub>/hBN flakes are deposited, are mounted to a custom SEM sample stub with sample heating[47]. No additional treatments or surface coatings are required. The SHeM sample environment operates at high-vacuum ( $\sim 2 \times 10^{-8}$  mbar) pressures.

## S2.3 - Measurement procedure

Each sample was heated to 220°C for 2 hours to ensure the removal of surface contaminants from the MoS<sub>2</sub>, which helium has a high sensitivity to. Prior to heating, diffractive measurements of the samples were attempted and yielded disordered scattering rather than ordered diffraction, as one would expect from a surface covered in disordered adsorbates. Helium has a large scattering cross-section for physisorbed (van der Waals bound) surface adsorbates, due to the low energy of the atoms and a strong attractive component in its interaction potential. Therefore, even low coverages of surface adsorbates will create predominantly disordered scattering. After heating, the same measurements were repeated and showed the expected diffraction corresponding to the trigonal arrangement of the top sulphur atoms. Diffraction scans along a principal azimuth were taken whilst passively cooling the native defect density sample from 220-40°C to characterise diffraction peak position and width as a function of temperature, shown in figure S2 (SI). All subsequent defect density measurements were taken at a temperature of 120°C to ensure that vacuum contaminants would not re-adsorb to the sample.

To quantify defect density, SHeM diffraction measurements were performed on each sample and the ratio of detected helium intensity which exhibits ordered vs. disordered scattering used to determine the degree of order present on the sample surface. In figure 2, the diffraction patterns of the two extrema of surface order are shown. The pristine bulk MoS<sub>2</sub> and pristine monolayer MoS<sub>2</sub>/hBN/SiO<sub>2</sub> represent the maximum ‘order’ achievable in the presented samples, and conversely, the pristine monolayer MoS<sub>2</sub>/SiO<sub>2</sub> represents the minimum (via substrate interaction). Due to real-world experimental constraints, there will always be some disordered background signal detected arising from multiple scattering[14], [48], [49] and imperfect samples (e.g.  $> 0 \text{ cm}^{-2}$  defect density). By including bulk MoS<sub>2</sub>/SiO<sub>2</sub> and exposed SiO<sub>2</sub> on each sample one can perform normalisation measurements to determine the amount of disordered scattering background signal to subtract it from diffraction measurements of the defective sample. A detailed discussion of the procedures used to subtract background signal and normalise detected signal across different samples is contained in the Supplementary Information.

## S2.4 - Lattice constant measurement in monolayer

Figure S1 shows the raw 2D diffraction data acquired from the monolayer MoS<sub>2</sub>. Diffraction peak locations were identified (with the exception of specular which is at the centre of the plot) by fitting a 2D Gaussian and 2<sup>nd</sup> order polynomial background to each peak – the same model as used by von Jeinsen et al.[19] Initial guesses of the peaks are shown in red on the figure, while the fitted locations are in blue. All the spacings were averaged, with the standard error being calculated for that average (the number of independent measurements was taken to be the number of diffraction peaks used).

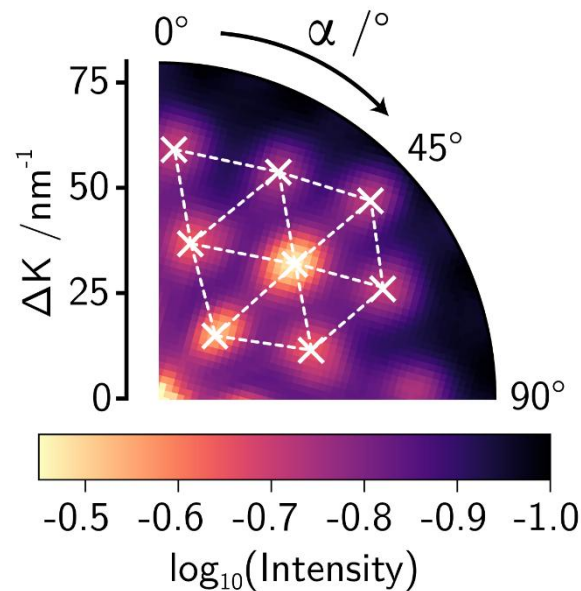


**Figure S1 – Determining the lattice constant of ML-MoS<sub>2</sub>:** Plot of 2D Bragg diffraction for native defect density monolayer MoS<sub>2</sub> with the principal azimuth ( $\langle 10 \rangle$ ) lying along  $\alpha = 45^\circ$  and measured at 373K. The average of distances (dashed lines) between adjacent peaks (crosses) is then used to calculate the lattice constant,  $a = 3.20 \pm 0.07 \text{ \AA}$ . Literature values are  $\sim 3.16 \text{ \AA}$  [31]. The centres of diffraction peaks were identified using 2D Gaussian fitting.



## S2.5 - Temperature dependence of helium atom micro-diffraction

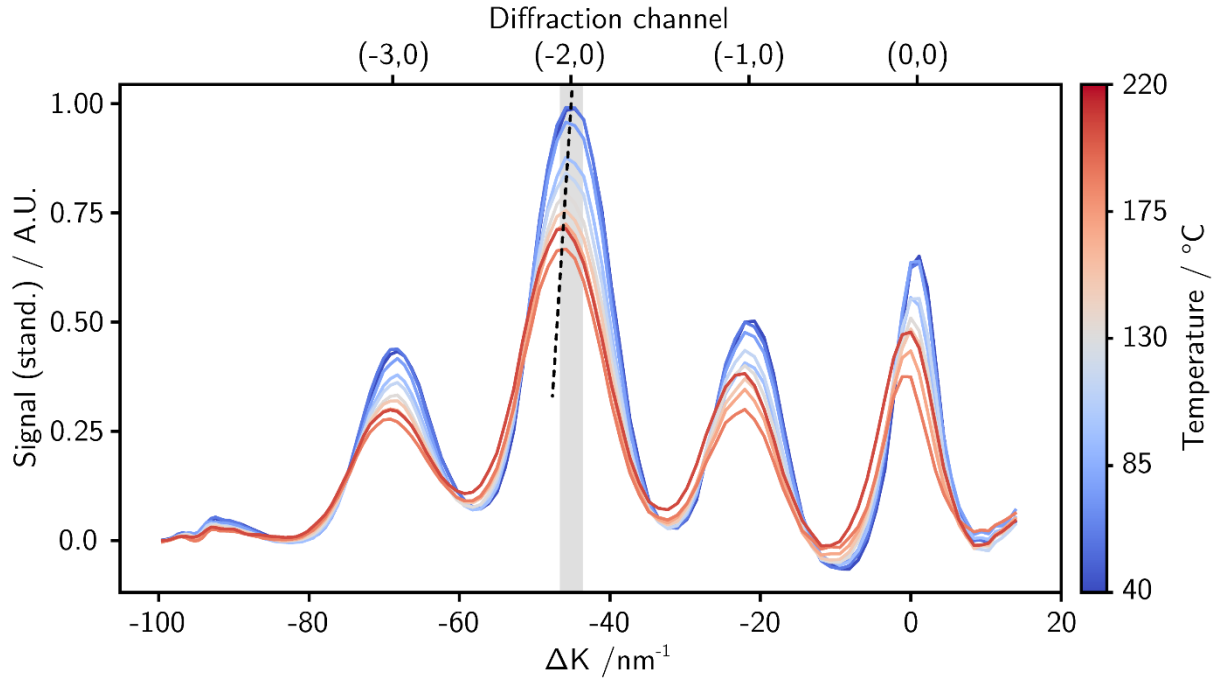


**Figure S2 – Temperature dependence of helium atom micro-diffraction:** Line scans of the native defect density ML-MoS<sub>2</sub> taken along a principal azimuth to characterize the relationship between Bragg intensity and temperature in helium-MoS<sub>2</sub> scattering, known as the Debye-Waller factor. A dashed line to guide the eye highlights the decreasing diffraction peak intensity, and migration towards larger momentum transfers ( $\Delta K$ ), as temperature increases. The  $I \propto 1/T$  proportionality is captured by  $I/I_0 = \exp(-2TW)$  where the Debye-Waller factor is  $2W$ . One could calculate the electron-phonon coupling constant using the Debye-Waller factor [39], [58].

## S2.6 – Measuring defect density as a function of temperature – 120°C vs 200°C

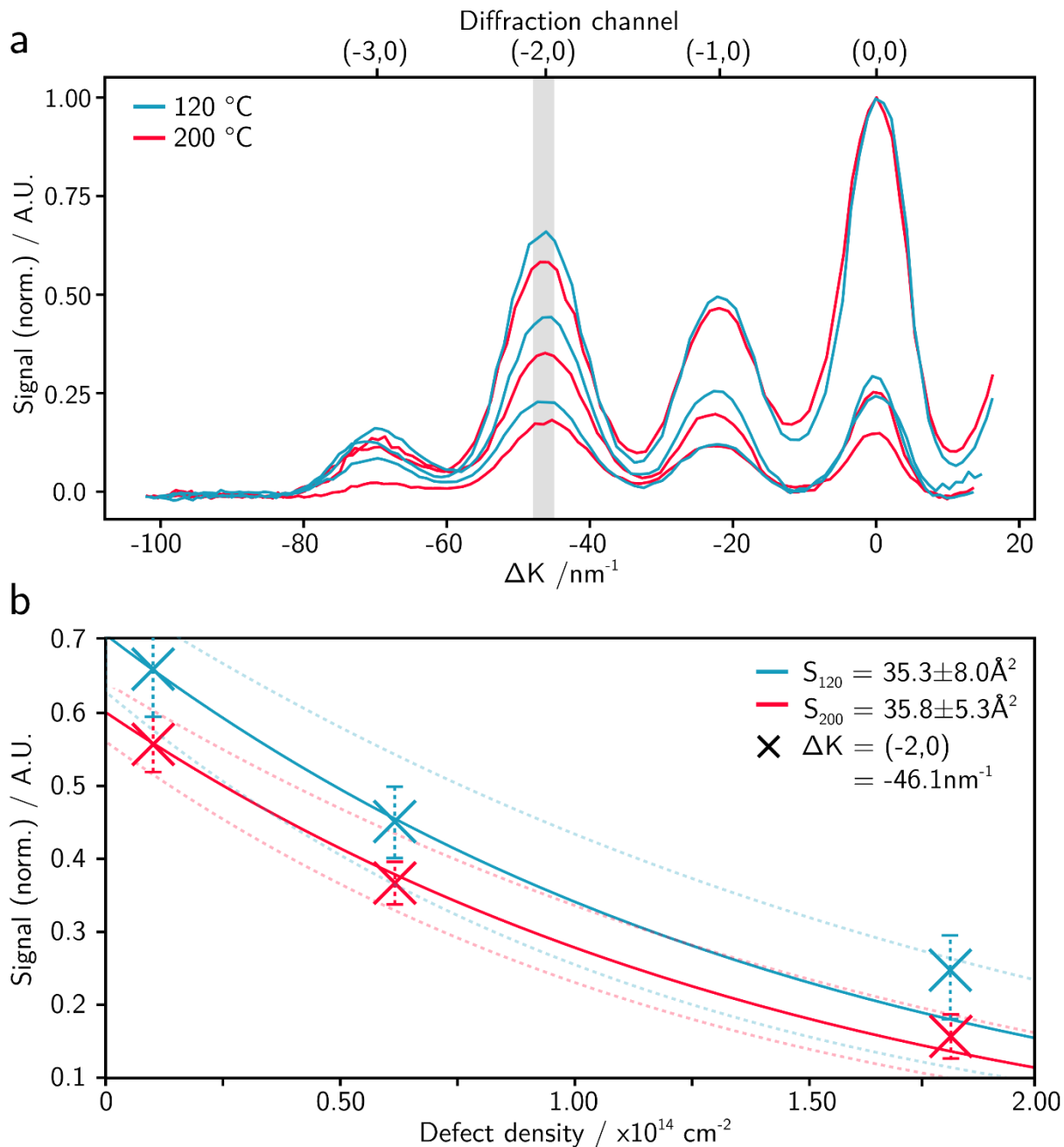


**Figure S3 – Quantifying defect density in ML-MoS<sub>2</sub> at different temperatures:** Panel (a), line scans of increasing defect density monolayer MoS<sub>2</sub> showing a consistent decrease in diffracted intensity as defect density increases at 120°C and 200°C. 200°C is the same as in figure 4. Panel (b) shows intensities extracted using Gaussian fitting to the (-2,0) diffraction peaks at both temperatures and strong agreement with the lattice gas model from equation 1 in both cases. Solely considering the effect of temperature on Bragg diffraction, according to Debye-Waller attenuation, the lower temperature should have increased intensity in ordered scattering, thereby decreasing experimental errors. This neglects the possibility that vacuum contaminants will also adsorb to the surface more readily at lower temperatures, reducing the degree of order and introducing cosine-like (diffuse) rather than Bragg-like scattering.

## S2.7 – Lattice gas model applied to the (-1,0) diffraction peak

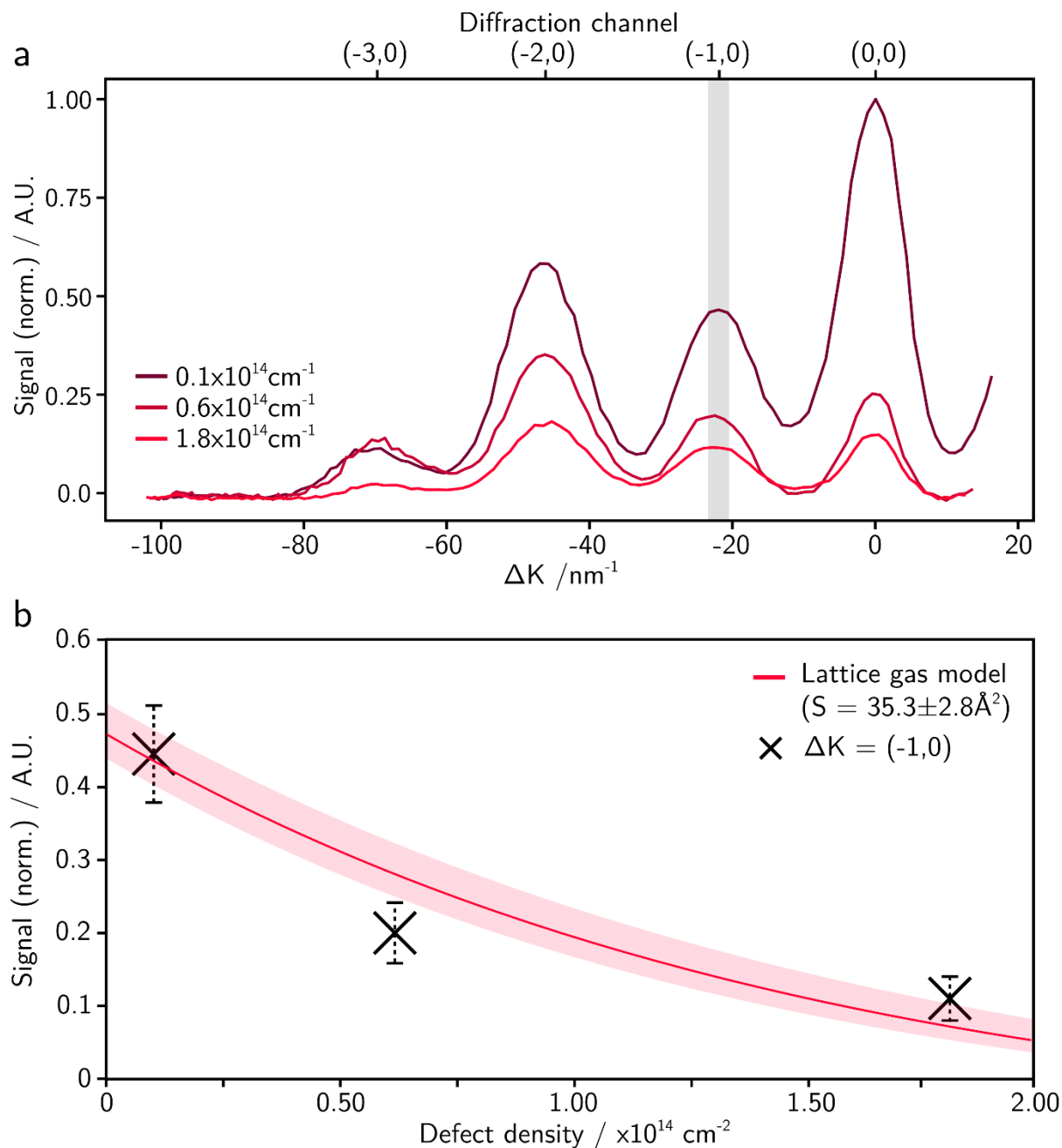


**Figure S4 – Quantifying defect density using the (-1,0) Bragg peak:** Panel (a), line scans of increasing defect density monolayer  $\text{MoS}_2$  acquired at  $200^\circ\text{C}$  showing a consistent decrease in diffracted intensity as defect density increases, as previously shown in figure 4. Panel (b) shows intensities extracted using Gaussian fitting to the (-1,0) diffraction peaks and qualitative agreement with the lattice gas model from equation 1. The (-1,0) peak suffers from lower intensities and an increased sensitivity to sample tilt compared to (-2,0), which negatively effects the quality of the fit.

## S3 – Computational methods

### S3.1 - Modelling

Full simulation of SHeM measurements, in both real and reciprocal space, is possible using ray tracing if an accurate scattering distribution is known[48], which can be determined by simulating the He-surface interaction potential. Here, we first use density function theory (DFT) to generate a physically accurate, but spatially sparse, He-surface and He-defect interaction potentials. These sparse points are then used to fit an analytical form of the defect-free MoS<sub>2</sub> potential energy surface (PES), and of the He-defect interaction potential. To model a defective sample of MoS<sub>2</sub>, the pristine PES is generated for an area of MoS<sub>2</sub> several unit cells in size. Under the assumption that the physical sizes of the defects do not physically overlap (lattice gas equation), the He-defect potentials can be inserted additively into a defect-free MoS<sub>2</sub> surface.

These potentials are then supplied to a close-coupled method [50], [51] to determine the scattering probabilities of helium atoms into particular outgoing directions. Having defined a scattering distribution, in-house Monte Carlo ray-tracing simulations were applied [48], [52] to evaluate the expected HAMD contrast.

In this section we outline how each of these interaction potentials is determined, the theoretical effect of defect density on the scattering distribution which in turn predicts the relationship between Bragg diffraction and defect density.

We assume a defect-free ( $\Theta = 0$ ) potential of the form,

$$V(x, y, z) = V_S(z)Q(x, y) + V_H(z)Q\left(x, y - \frac{c}{\sqrt{3}}\right) + V_M(z)Q\left(x - \frac{c}{2}, y - \frac{c}{2\sqrt{3}}\right) \quad (2)$$

where  $c$ , the lattice parameter of MoS<sub>2</sub>,  $Q$  is the corrugation function and  $V_i$  is the combined repulsive and Morse potential where the indices S, H and M represent sulphur, molybdenum and hollow sites, respectively, marked by the blue, green and red points in figure S3.1. The hexagonal corrugation function takes the form,

$$Q(x, y) = \frac{2}{9} [\cos(x' - y') + \cos(2y') + \cos(x' + y' + 3\pi)] \quad (3)$$

where  $x' = 2\pi \frac{x}{c}$ ,  $y' = 2\pi \frac{y}{c\sqrt{3}}$ , such that at specific site  $i$  all other terms vanish from the total potential and  $V = V_i$ . The combined repulsive and Morse potential takes the form,

$$V = D [\exp(2\alpha(z_0 - z)) - 2a \exp(\alpha(z_0 - z)) - 2b \exp(2\beta(z_1 - z))] \quad (4)$$

Where  $D_i, a_i, b_i, \alpha_i, \beta_i, z_0, z_1$  are empirical parameters that are determined from fitting to a DFT potential at the three possible sites (S, H, M). The values of all parameters in the potential are shown in Table S3 below

Site / i	$D / \text{meV}$	$a$	$b$	$\alpha / \text{\AA}^{-1}$	$\beta / \text{\AA}^{-1}$	$z_0 / \text{\AA}$	$z_1 / \text{\AA}$
Sulphur	20.0	0.812	0.196	1.44	0.203	3.37	1.73
Molybdenum	20.1	1.00	0.0026	1.15	1.24	3.22	4.19
Hollow	25.0	0.464	0.199	1.10	0.648	3.14	3.82

**Table S3 – Empirical potential energy surface parameters describing pristine He-MoS<sub>2</sub>:** Parameters describing the total, pristine He-MoS<sub>2</sub> interaction potential determined from fitting to DFT calculated sites.

We define the potential at the defect site,  $V_{\text{defect}}(z)$ , as

$$\begin{aligned}
 V_{\text{defect}}(z) = & d[\exp(2\gamma(z_2 - z)) - 2c \exp(\gamma(z_2 - z)) - 2e \exp(2(z_3 - z))] \\
 & - 2c \exp(\gamma(z_2 - z)) \\
 & - 2e \exp(2\lambda(z_3 - z))], \quad (5)
 \end{aligned}$$

Where  $d, c, e, \gamma, \lambda, z_2, z_3$  are parameters fitted to a DFT He-defect potential to find the values in Table S4 below.

$d / \text{meV}$	$c$	$e$	$\gamma / \text{\AA}^{-1}$	$\lambda / \text{\AA}^{-1}$	$z_2 / \text{\AA}$	$z_3 / \text{\AA}$
32.8	0.0311	16.4	0.921	0.924	5.60	3.71

**Table S4 – Empirical potential energy surface parameters describing the sulphur vacancy defect site for He-MoS<sub>2</sub>:** Parameters describing the He-defect interaction potential determined from fitting to DFT.

All DFT calculations presented in this work were performed using CASTEP [53], a plane-wave-based DFT code employing periodic boundary conditions. The exchange-correlation energy was treated using the Perdew–Burke–Ernzerhof (PBE) [54] functional within the generalised gradient approximation, with DFT-D3 [55] dispersion corrections included to account for van der Waals interactions. A kinetic energy cutoff of 600 eV was used for the plane-wave basis set, and ultrasoft pseudopotentials [56] were employed for all elements. To eliminate spurious interactions between periodic images, a vacuum spacing of 25 Å was introduced along the out-of-plane direction. A  $4 \times 4 \times 1$  supercell of MoS<sub>2</sub> was used to prevent artificial interactions between adjacent He atoms. The interaction energy between a single helium atom and the MoS<sub>2</sub> surface was evaluated under the rigid-surface approximation, where the helium atom is assumed not to significantly perturb the substrate structure. Accordingly, the MoS<sub>2</sub> slab was fully relaxed first, and the He atom was subsequently placed at selected sites above the surface for single-point total energy calculations. A  $4 \times 4 \times 1$  Monkhorst–Pack [57] k-point mesh was used. Electronic energy convergence was set to  $1 \times 10^{-8}$  eV, and a force convergence criterion of 0.03 eV/Å was applied during structural relaxations. The sites where the He atom was placed coincided with the S, H and M atomic sites which allowed all parameters of each of the potentials  $V_i$  to be fitted, from which the PES across the entire surface could be evaluated using equation 4.

We can now use the total He- MoS<sub>2</sub> potential, that includes a defect term (both potentials are shown in figure S3.1), to calculate the expected helium flux that will be scattered into discrete diffraction channels as shown in figure S6.

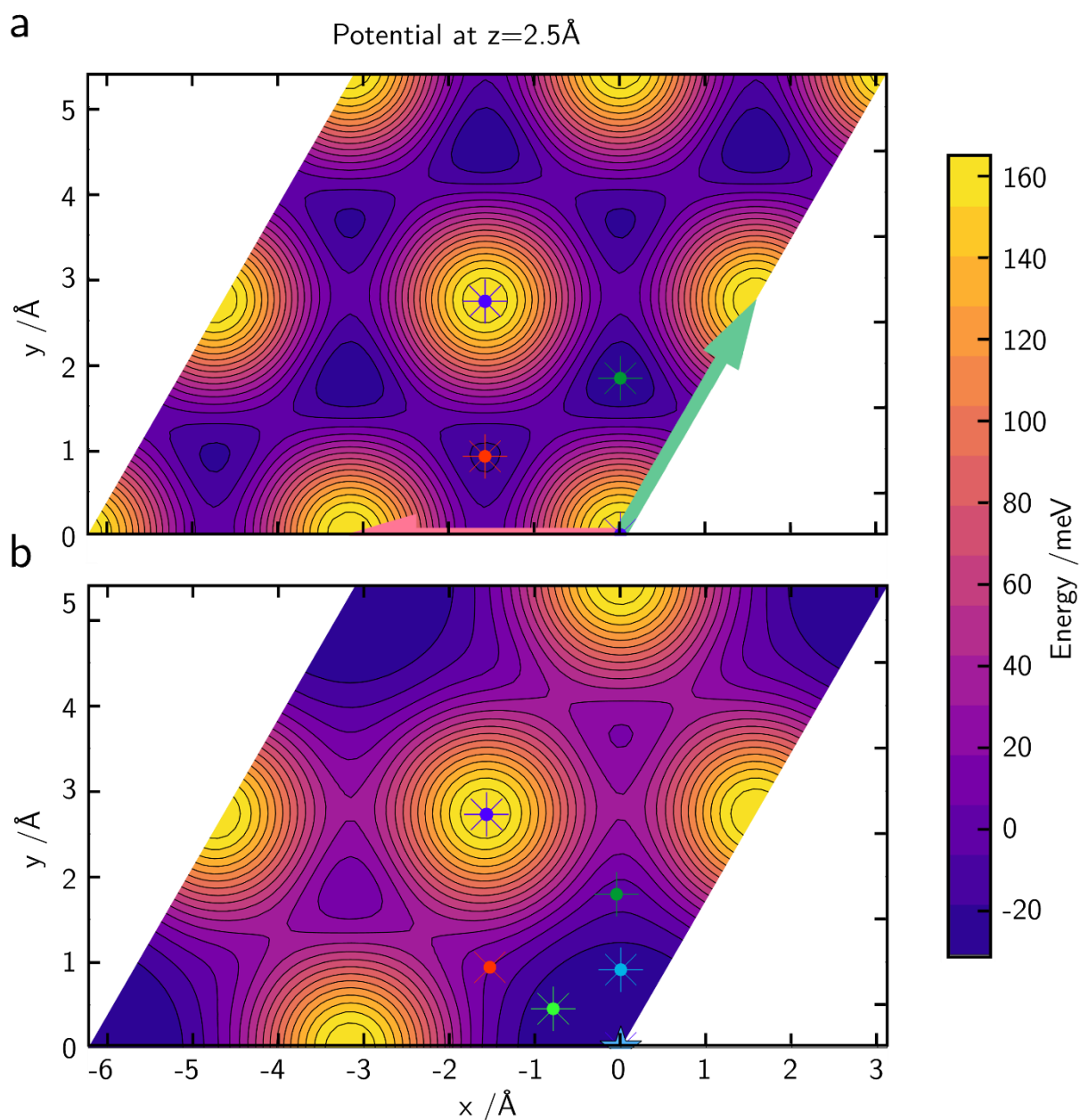


**Figure S5 – Pristine and defective He-MoS<sub>2</sub> potential energy surfaces:** He-MoS<sub>2</sub> potential energy surfaces of (a) pristine and (b) defective MoS<sub>2</sub> at a height  $z = 2.5\text{\AA}$  from the top sulphur ionic cores, approximately the classic turning point of an incident helium atom with thermal energy. The light regions represent sulphur atoms and the dark regions are hollow or molybdenum sites. Green dots mark hollow sites and red dots mark molybdenum atoms. The pink and green arrows in (a) show the real-space lattice vectors. In (b) a sulphur vacancy is marked with a blue star at  $(x, y) = (0, 0)\text{\AA}$ .



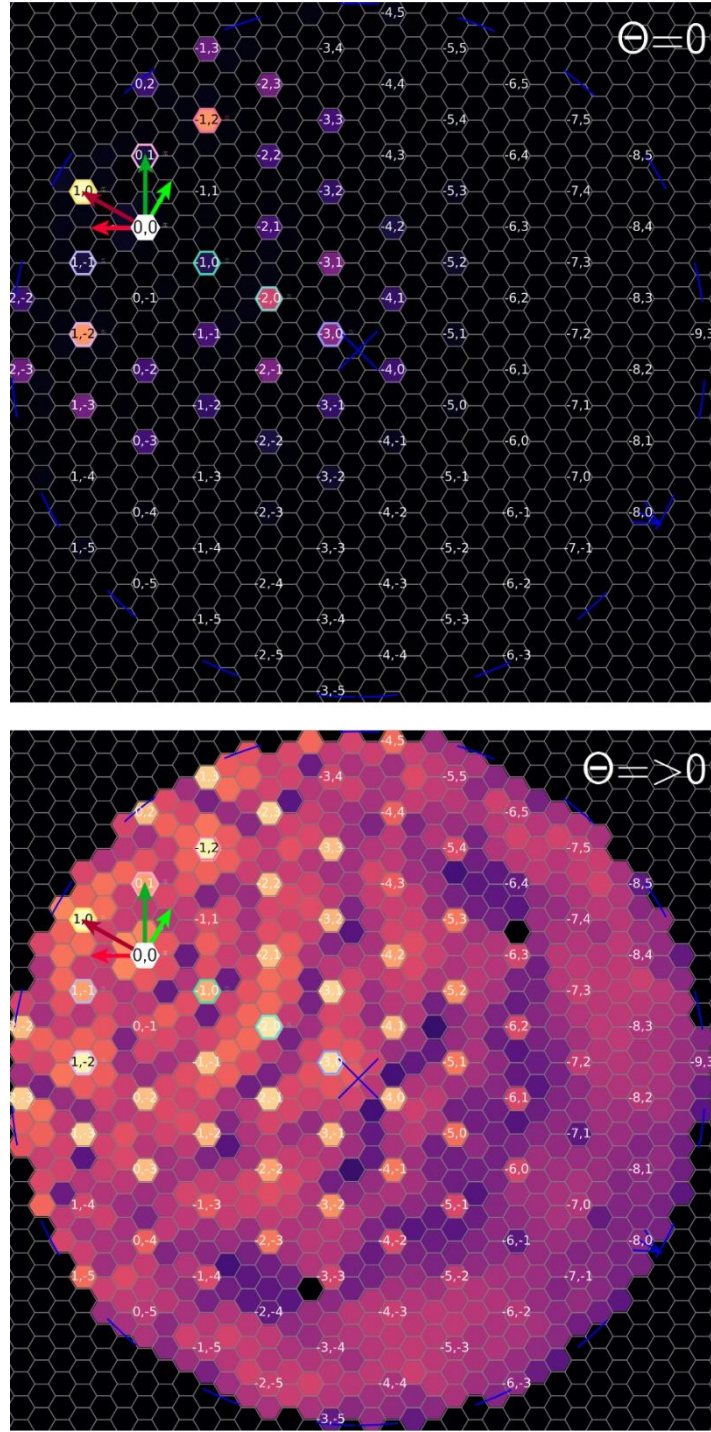


**Figure S6 – Modelling the effect of defect density on helium atom micro-diffraction:** Reciprocal/momentum-space scattering distributions of defect-free (a) and defective (b) MoS<sub>2</sub> potential energy surfaces (PES) (shown in figure S3.1) calculated using a close-coupled method to solve matter-wave scattering using the time-dependent Schrodinger equation [50], [51]. Using the defect-free PES the outgoing scattered flux is confined to kinematically allowed ( $\mathbf{k}_f = \mathbf{k}_i + \mathbf{G}$ , where  $\mathbf{k}$  is the incoming/outgoing wavevector and  $\mathbf{G}$  is the reciprocal lattice vector) diffraction channels (ones with integer coordinates in reciprocal space), constituting solely ordered diffraction. By introducing a defect to the PES the scattered flux becomes disordered and begins to populate kinematically forbidden ( $\mathbf{k}_f \neq \mathbf{k}_i + \mathbf{G}$ ) channels, introducing disordered, cosine-like scattering. Reciprocal-space lattice vectors are shown in dark red/green, with their real-space counterparts in light red/green. The specular scattering condition ((0,0) channel) is off-centre to reflect the 45° incidence scattering geometry in the experimental SHeM set-up used in the current work. The blue cross represents the outgoing wavevector normal to the sample surface. As defect density increases, the average outgoing wavevector will migrate from near the specular (0,0) condition towards the blue cross.